Holographic Measurements of Transition and Turbulent Bursting in Supersonic Axisymmetric Boundary Layers

A. George Havener*
University of Dayton, Dayton, Ohio

Holographic interferometric density and velocity data of laminar and turbulent boundary layers, plus boundary-layer transition and turbulent bursting on sharp-tip cones in supersonic high Reynolds number airflows, are presented. Development of an improved numerical data-reduction process that minimizes the adverse effects of anomalies in interferometric measurements is also presented. From dual-plate holography, a special form of phase-shift interferometry is used to measure the fringe shifts, and by using a microcomparator to view the object waves directly as they are reconstructed from the holograms, a practical measuring resolution of 15 μm is obtained. This resolution is demonstrated by measuring eight fringe shifts for an 0.11 mm thick laminar boundary layer and again by measuring 66 fringe shifts for a turbulent boundary layer that is approximately 1.0 mm thick. These data are reduced to density and velocity distributions that are compared to theory to assess the relative error in the optical measurements.

Nomenclature

A,B,C,a,b,c	= constants as applicable
c_p	= specific heat, constant pressure
D	= reference fringe spacing
$f(r)$	= radial density function
G	= optical constant, $K_{DG}\rho_{ref}/\lambda$
h	= enthalpy
K_{DG}	= Dale Gladstone constant
l	= local fringe displacement
M	= Mach number
N	= nodes
Pr	= Prandtl number
n	= index of refraction
R	= maximum field boundary
R_g	= ideal gas constant, air
Re	= Reynolds number
r	= radial coordinate
S	= measured fringe shift, l/D
$S(y)$	= fringe-shift function
$S'(y)$	= dS/dy
T	= temperature
V	= velocity
x,y,z	= space coordinates
η	= transform coordinate for r: $\eta = 1-(r/R)^2$
λ	= wavelength of light
ζ	= transform coordinate for y: $\zeta = 1-(y/R)^2$
ρ	= density

Subscripts

e	= edge of boundary layer
i	= specific light ray
npt	= number of measured fringe shifts
0	= total condition
r	= condition at arbitrary radius
ref	= condition for $y>R$
s	= adiabatic stagnation state
w	= wall condition
∞	= freestream condition
aw	= adiabatic wall condition
1,2,3,...	= positions or fringe number as applicable
I	= boundary-layer flowfield
II	= inviscid flowfield

Presented as Paper 83-1724 at the AIAA 16th Fluid and Plasma Dynamics Conference, Danvers, MA, July 12-14, 1983; received June 22, 1987; revision received Feb. 16, 1988.

*Associate Professor, Department of Mechanical Engineering; currently, Principal Engineer, CALSPAN/AEDC Operations, Arnold Air Force Base, TN. Associate Fellow AIAA.

Introduction

NEW results from a holographic interferometric study on axisymmetric supersonic air boundary layers and turbulent bursting are presented. In addition to these new data, some important problems pertinent to reducing interferometric data of real, unsteady, axisymmetric flows are resolved. These problems are 1) acquisition of sufficient interferometric data, particularly for weak phase fields (as used here, weak phase fields are regions in the boundary layers where the total fringe shift is less than one); 2) reliable resolution of the interferometric measurements without amplifying anomalies in the data; and 3) analyses of fields that have complex density distributions. The problem of coping with insufficient optical data is resolved by using a special form of phase-shift interferometry; the problem of numerical data processing is resolved by using a delayed differentiation process, and the problem associated with complex fields is resolved by using a method for isolating fields that are interior to central fields. Direct application is made to studies of supersonic boundary-layer flows on sharp-tip cones at zero angle of attack.

Theory

Optical path lengths through refractionless, axisymmetric flowfields are related to density[1-4,6-10] by

$$S(y) = 2G\int_y^R \frac{f(r)r}{\sqrt{r^2-y^2}}\,dr \tag{1}$$

Measurable changes in optical path lengths are fringe shifts visible in interferograms of the flowfield. The function $S(y)$ describes the fringe shifts for light rays traversing the field in the z direction (Fig. 1), and $f(r)$ is defined as

$$f(r) = [\rho(r)/\rho_{ref}] - 1$$

For flowfields that are piecewise continuous at $r = R$ such that $\rho(R^-) = \rho_1$ and $\rho(R^+) = \rho_{ref}$, $f(r)$ is redefined to account for

the discontinuity

$$f(r) = \frac{\rho(r) - \rho_1}{\rho_{\text{ref}}} + \frac{\rho_1}{\rho_{\text{ref}}} - 1 \tag{2}$$

where $\rho_{\text{ref}} f(R) = \rho_1 - \rho_{\text{ref}}$, the step change in the density at $r = R$. Bennett et al.[1] describe other forms of reduced density functions for flowfields with piecewise continuous density distributions. In practice, $S(y)$ is obtained from interferometric measurements of the flowfield, after which $f(r)$ is computed from the inversion of Eq. (1)

$$f(r) = -\frac{1}{G\pi} \int_y^R \frac{S'(y)}{\sqrt{y^2 - r^2}}\, dy \tag{3}$$

A major difficulty with Eq. (3) is the treatment of $S'(y)$. If $S(y)$ were known as an analytic function for real flows, the use of Eq. (3) would be trouble free, but as the S data are empirical, $S(y)$ has to be determined carefully so that scatter in the measurements of S is not amplified by $S'(y)$. The mathematical inversions of Eq. (3) that are reported in the literature[2] are usually affected adversely by $S'(y)$. In this study, a method based on those of Barr[3] and Bradley[4] is developed, and it is found to be significantly less sensitive to $S'(y)$ in direct application to wind-tunnel tests of supersonic airflows. Briefly, in this method, the differentiation and integration steps are reversed, and the inverted form of Eq. (1) is applied to individual segments rather than to the entire field. Final calculation for $f(r)$ is made by summing the results of all segments applicable to y. Reversing the order of the calculus steps permits natural smoothing of the data prior to coping with $S'(y)$, and application to individual segments diminishes the influences that errant measurements of S may have on the entire field.

Modified Delayed Differentiation Method

If we use the transformations of Bradley, Eq. (1) becomes

$$S(\zeta) = GR \int_0^\zeta \frac{f(\eta)}{\sqrt{\zeta - \eta}}\, d\eta \tag{4}$$

If we follow Hildebrand,[5] an inversion of Eq. (4) is

$$f(\eta) = \frac{1}{GR\pi} \frac{d}{d\eta} \int_0^\eta \frac{S(\zeta)}{\sqrt{\eta - \zeta}}\, d\zeta \tag{5}$$

To evaluate Eq. (5), the field of Fig. 1 is partitioned into coaxial regions of arbitrary width, each of which contains four S measurements. Nodes designate the boundaries separating adjacent regions; N_1 is the node at $y = R$. Numerical determination of $S(\zeta)$ for each region is a best-fit parabola to the boundary nodes of the region plus the two interior points. Next, the integral of Eq. (5) is evaluated for each measurement of S, and the calculation is completed by multiplying the derivative of the integral by $1/GR\pi$. For each η, the derivative of the integral function in Eq. (5) is determined from a best-fit parabola of three values to the left and right of η plus η itself.

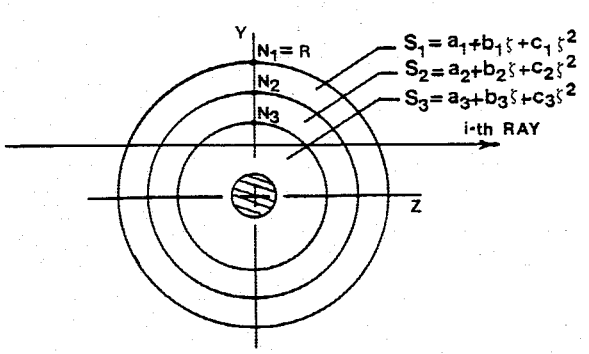

Fig. 1 Nomenclature for axisymmetric optical phase field.

At the extremities of the field, the first seven (or last seven) values are used to compute the initial three (or latter three) densities.

To illustrate, consider the axisymmetric, partitioned field of Fig. 1. The shaded region denotes a solid object in the field. As illustrated, the ith light ray passes through three coaxial regions of the flow. A least-squares algorithm is used to determine the coefficients (a,b,c) for the parabolic $S(\zeta)$ distributions of each region. If we denote $F(\eta_i)$ as the value of the integral function in Eq. (5), $F(\eta_i)$ is

$$\begin{aligned} F(\eta_i) &= 2[a_1 + (2/3)b_1\eta_i + (8/15)c_1\eta_i^2]\sqrt{\eta_i} \\ &+ 2(a_3 - a_2)\sqrt{\eta_i - N_2} + 2(a_2 - a_1)\sqrt{\eta_i - N_1} \\ &+ 2(b_3 - b_2)[N_2 + (2/3)(\eta_i - N_2)]\sqrt{\eta_i - N_2} \\ &+ 2(b_2 - b_1)[N_1 + (2/3)(\eta_i - N_1)]\sqrt{\eta_i - N_1} \\ &+ 2(c_3 - c_2)[N_2^2 + (4/3)(\eta_i - N_2) + (8/16)(\eta_i - N_2)^2] \\ &\times \sqrt{\eta_i - N_2} + 2(c_2 - c_1)[N_1^2 + (4/3)(\eta_i - N_1) \\ &+ (8/16)(\eta_i - N_1)^2]\sqrt{\eta_i - N_1} \end{aligned} \tag{6}$$

The terms containing a_1, b_1, and c_1 are the contributions from the outermost region, and the other coefficients are for the respective inner regions. When a fourth region is involved, N_4 is the next node, and three additional terms are added to Eq. (6)

$$\begin{aligned} &2(a_4 - a_3)\sqrt{\eta_i - N_3} \\ &+ 2(b_4 - b_3)[N_3 + (2/3)(\eta_i - N_3)]\sqrt{\eta_i - N_3} \\ &+ 2(c_4 - c_3)[N_3^2 + (4/3)N_3(\eta_i - N_3) \\ &+ (8/16)(\eta_i - N_3)^2]\sqrt{\eta_i - N_3} \end{aligned}$$

where the coefficients a_4, b_4, and c_4 pertain to

$$S_4 = a_4 + b_4\zeta + c_4\zeta^2$$

To complete the calculation, the derivative of the $F(\eta)$ data for the ith light ray is determined numerically, after which the density function is computed from

$$f(\eta_i) = (B + 2C\eta_i)/GR\pi \tag{7}$$

where B and C are coefficients of a best-fit parabola centered on the $F(\eta_i)$ subset of $[\eta_{i-3}, \eta_{i+3}]$; as previously stated, the initial three $f(\eta)$, or latter three values, are based on the subsets $[\eta_1, \eta_7]$ or $[\eta_{\text{npt}-7}, \eta_{\text{npt}}]$, respectively. Figure 2 illustrates the procedure for computation of $f(\eta_9)$. The subset $[\eta_6, \eta_{12}]$ is used to determine the parabola $F(\eta_9) = A + B\eta_9 + C(\eta_9)^2$, and, subsequently, $f(\eta_9) = (B + 2C\eta_9)/GR\pi$.

Description of Nested Axisymmetric Fields

Equation (1) shows that for $y < R$, the optical path length through the field depends on the structure of the density field integrated across the secant at y_i. When the density field is homogeneous and aptly modeled by an analytic function (e.g., simple inviscid flowfields), $S'(y)$ is continuous, and the inversion of Eq. (1) is direct. To determine $f(r)$ for fields where the model for $S'(y)$ is discontinuous, the inversion technique is modified. The term "nested" pertains to axisymmetric fields for which $S'(y)$ is modeled as a piecewise continuous function. In general, nested fields are of two types, coaxial and embedded. Development and application of embedded fields are presented elsewhere.[6]

Nested coaxial fields are regions of different density layered about a central axis of symmetry. In real flowfields, the density

is everywhere continuous, but mathematical modeling requires $S'(y)$, or both $S'(y)$ and $f(r)$, to be discontinuous at the interfaces. The axisymmetric flow about a sharp-tip cone in a uniform, supersonic airstream is an example (a segment of the interferogram of Fig. 3 is shown in Fig. 4). When adjacent density fields are patched together by the shock wave, both $S'(y)$ and $f(r)$ are modeled as mathematical discontinuities, while at the boundary-layer edge, $S'(y)$ alone is discontinuous. In Fig. 3, the ith ray through the field is drawn for an optical path that is influenced both by Region I, the viscous boundary layer, and Region II, the compressible inviscid field. The boundary-layer thickness is defined as the radius $r = y_e$ at which $S'(y)$ is discontinuous. For $y_i < y_e$, the fringe shift is $S(y_i) = S(y_i)_I + S(y_i)_{II}$; $S(y_i)_I$ is separated from $S(y_i)$ as

$$S(y_i)_I = S(y_i) - GR \int_0^{\zeta_e} \frac{f_{II}(\eta)}{\sqrt{\zeta - \eta}}\, d\eta \qquad (8)$$

The integral of Eq. (8) is the contribution of the inviscid field to the total fringe shift recorded in the interferogram. With $S(y_i)_I$ known from Eq. (8), $f_I(\eta_i)$ is computed according to Eqs. (6) and (7).

Dual-Plate Holographic Interferometry

Holography and many of its applications to flowfield studies are reported in the literature,[2,7-11] as is dual hologram interferometry.[9-11] For this study, the two holograms are adjusted to produce finite-fringe interferograms in which the fringes of the freestream flowfield ahead of the shock wave are normal to the cone axis. Figure 5 is a sketch of three typical finite-fringe interferograms for a section of the flowfield corresponding to Figs. 3 and 4, Here, the S data are to be measured for the X_c plane. At y_i, $S(y_i) = l/D$, where l is the amount the fringe is deflected from its vertical orientation at X_c, y_i. As illustrated, a single interferogram provides data for only two fringe shifts for Region II and approximately one fringe shift for Region I.

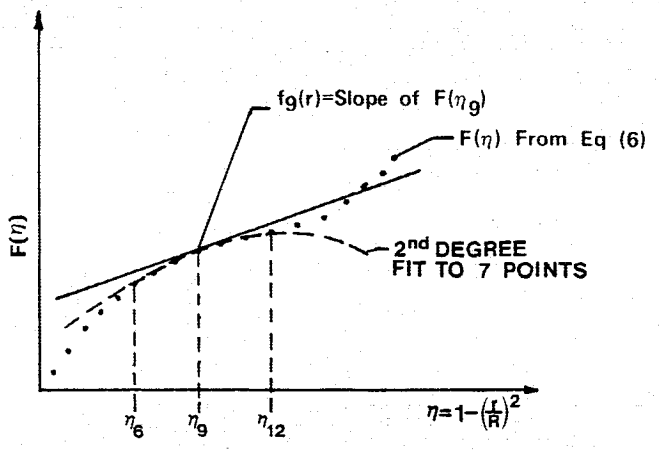

Fig. 2 Illustration for determination of the radial density function.

If the white fringes are also used, the measurable data are doubled, but even then the information is too little to obtain reliable descriptions for $S(y)$. If we use the dual hologram process, multiple interferograms of the same flowfield (only three are illustrated in Fig. 5) are obtained by carefully varying the alignment between the two holograms, and because each interferogram provides distinct measurements of S, the determination of $S(y)$ is improved. For example, at an X_c plane where the fringe shift for the laminar boundary layer is less than one, eight discrete fringe-shift measurements are obtained using this method (see Fig. 10).

Fundamentally, this process is a special case of discrete phase-shift interferometry,[12-14] because instead of monitoring changes in intensity as the optical phase of the field is varied continuously, only the locations of the null intensities (the centers of the dark fringes) are measured for specific planes normal to the axis of symmetry. Direct control on the formation of the interference pattern is the single most important feature of this application of dual hologram interferometry, because the micropositioning control on the alignment of the holograms provides sensitivity comparable to conventional Mach-Zehnder interferometry, and with the added use of piezo-electric crystal drives, relative fringe spacings and fringe orientations are controllable to within a fraction of a wave length.[9,10] As shown for the thin laminar boundary layer, this latter feature is particularly useful for the study of weak phase fields, because fractions of a fringe shift corresponding to fractions of a change in density are measurable. In principle, continuous measurement in either intensity or fringe shift is possible, but since the $S(y)$ values measured here are for the dark fringes only and are obtained by using a microcomparator to view the object waves directly as they are reconstructed from the holograms, a practical resolution of 15 μm, nominally, is realized.

Demonstration of this type of phase-shift interferometry is shown in Fig. 6, which is an array of interferograms as seen through the eyepiece of the microcomparator. The subject is a segment of a 12 deg half-angle cone in a nominal, Mach 3 flow. The gray region in the lower section of each photograph is the cone body, and the interferograms are of a portion of the inviscid field and the turbulent boundary layer. Flow is from left to right. The vertical straight fringes at the top are for the ambient $M = 3$ flow. The shock wave from the cone tip is seen as a sharp bending to the right of these reference fringes. The compressible inviscid flow is depicted by the monotonically curved fringes, and the boundary layer is shown as a sharp turn to the left of the inviscid flowfield fringes close to the cone surface. The cross hairs of the eyepiece are stationary with the upper cross hair positioned at y_e, and the lower cross hair is at an arbitrary point within the inviscid field. These six interferograms show one complete cycle of hologram adjustment. A cycle is a relative displacement of the holograms that causes one complete wavelength shift between the interferograms. The improvement here over earlier applications[10,11] of the dual-plate technique results from use of the traversable microcomparator to view directly the light waves reconstructed from the holograms and to measure directly the corresponding fringe shifts.

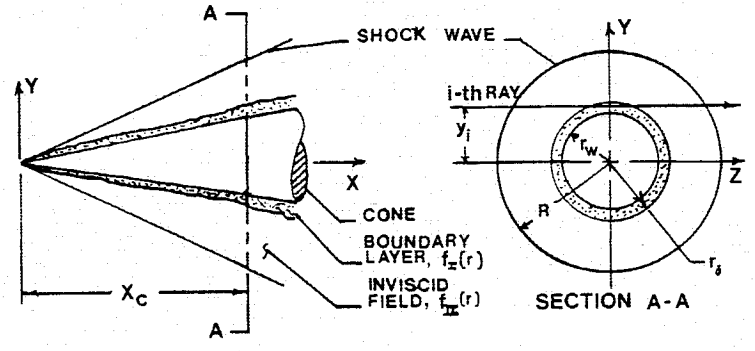

Fig. 3 Nomenclature for supersonic axisymmetric flowfield over a sharp-tip cone at zero angle of attack.

Inviscid Flowfield Results

Accuracy of the data-reduction process and fringe-measuring technique is determined by direct application to Region II. The S measurements for $X_c = 4.699$ cm are shown in Fig. 7, and Fig. 8 shows a comparison of four different data-reduction methods. The overall agreement between the S measurements and the theoretical fringe-shift distribution is good, but since the interferograms are instantaneous records of a turbulent

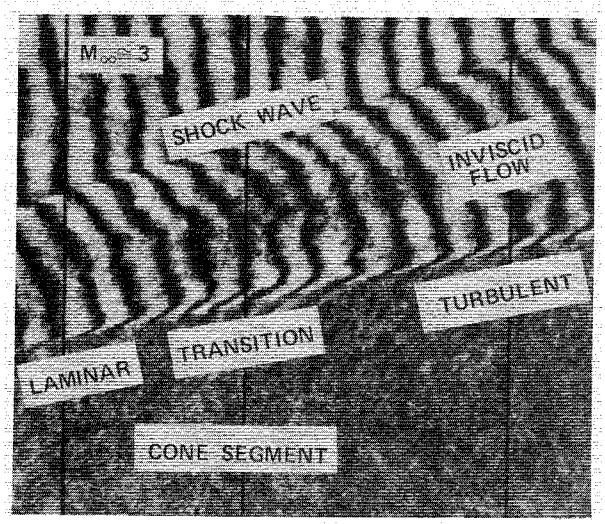

Fig. 4 Segment of holographic interferogram of flowfield of Fig. 3.

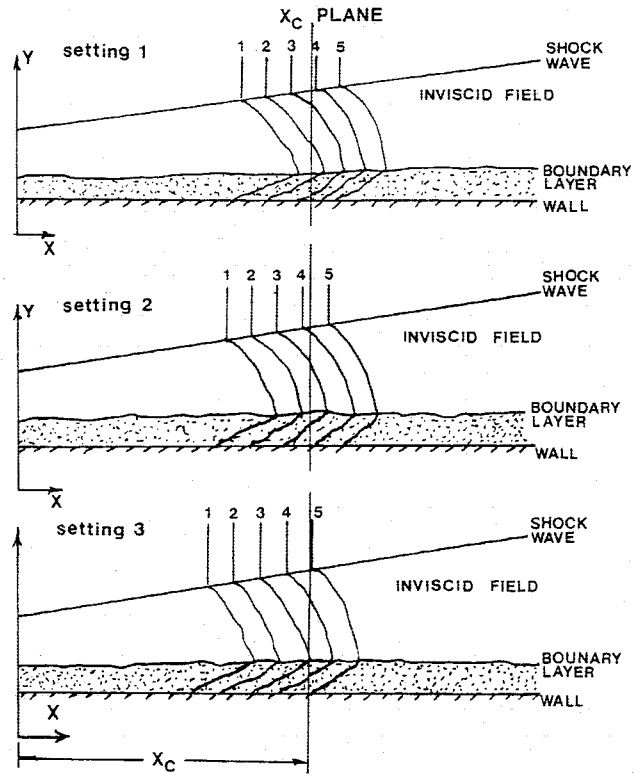

Fig. 5 Illustration of discrete phase shift interferometry.

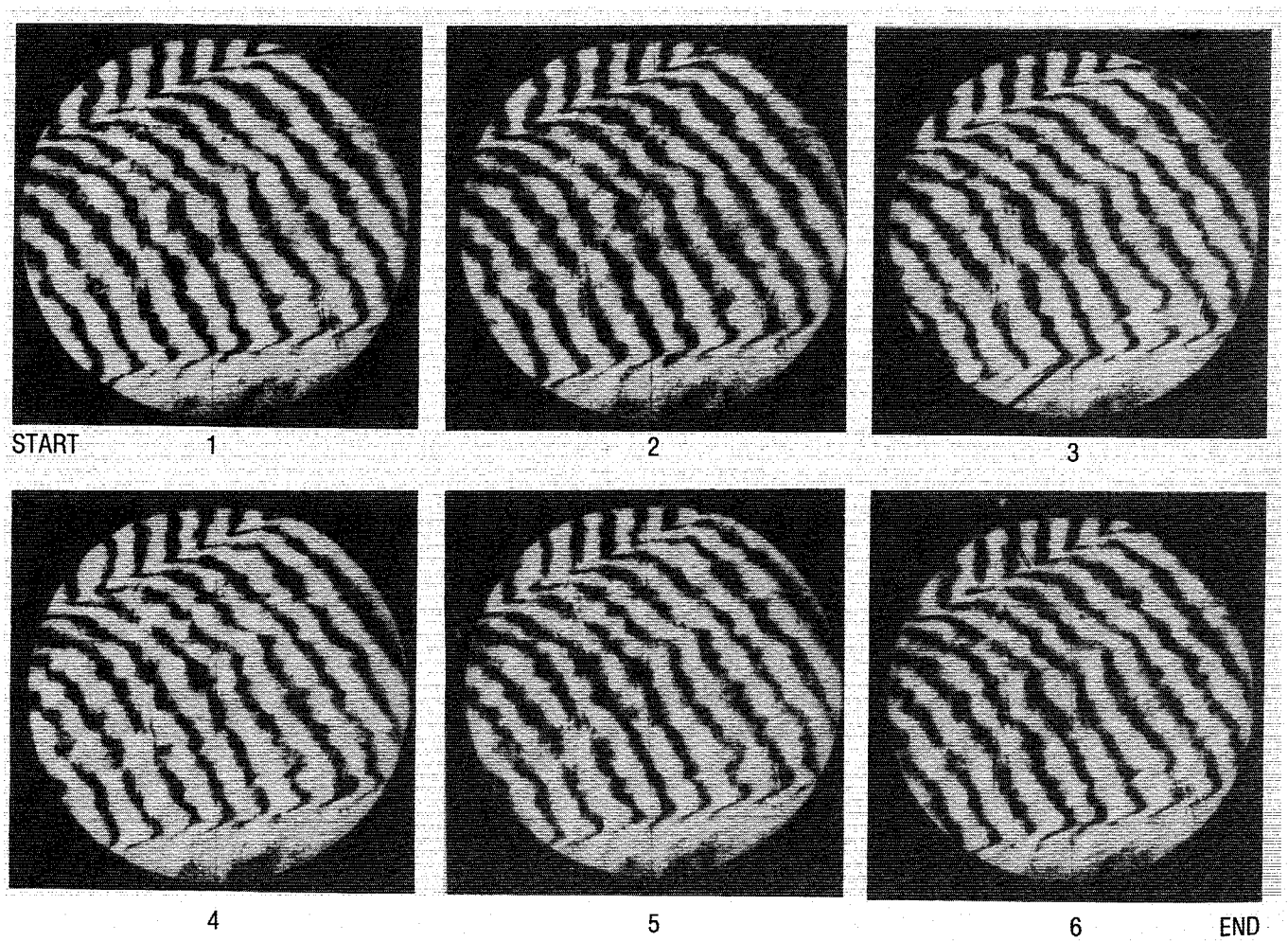

Fig. 6 Array of holographic interferograms demonstrating process of Fig. 5.

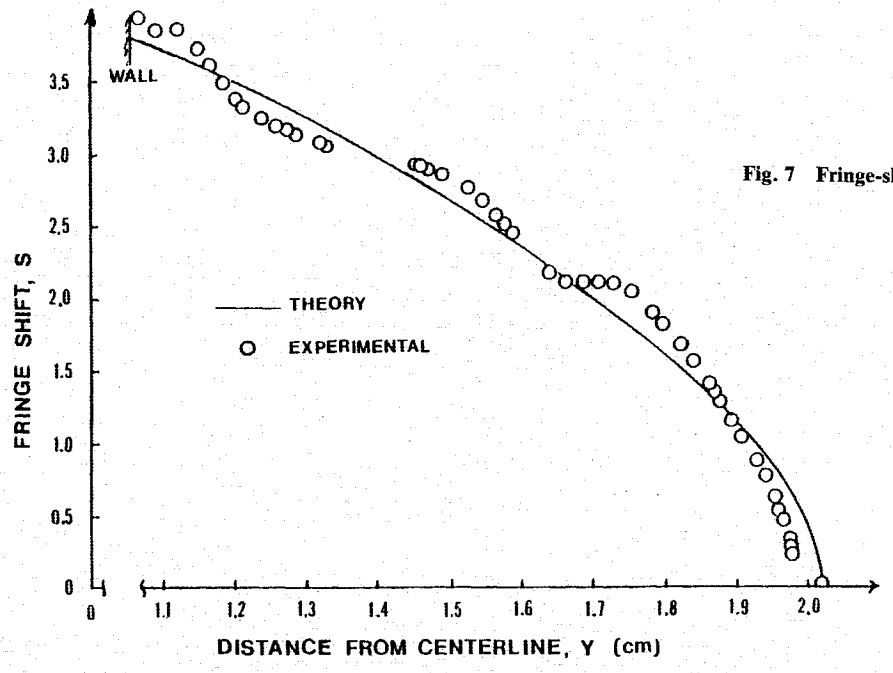

Fig. 7 Fringe-shift measurements of inviscid flowfield of Fig. 3.

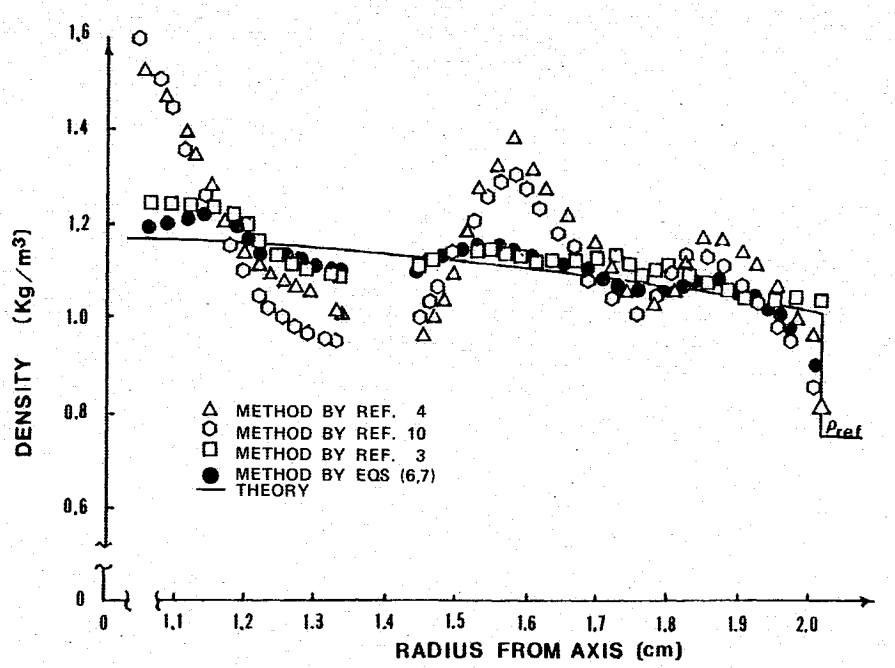

Fig. 8 Comparison of density data-reduction techniques applied to fringe-shift measurements of Fig. 7.

flow,[11] the unsteadiness is seen as scatter in the S measurements, and this scatter is a major problem to Eq. (5). If we use the methods of Refs. 4 and 10, the anomalies in the S data are magnified by $S'(y)$ to a level where the computed densities are unbelievable. Weighting factors and smoothing the S measurements can help, but, in general, coping directly with the $S'(y)$ of empirical data requires considerable smoothing or the use of large weighting factors, either of which merely forces the density data to collapse on an anticipated result. Noticeable improvement is seen by using Eqs. (6) and (7) or the method of Ref. 3. No weighting factors are used, and smoothing the S data occurs naturally from reversing the differentiation and integration steps. The method of Ref. 3 is not used or preferred here, because Eqs. (6) and (7) give better results at the inner boundaries of the regions, and because the numerical procedures of Ref. 3 require a priori partitioning of the field; no specific field partitioning is needed for the use of Eqs. (6) and (7). Note that since this flowfield is bounded by a shock wave that causes a step change in density at $y = R$, Eq. (2) is used to compute $f(r)$; ρ_1 is the density on the immediate downstream side of the shock wave predicted from inviscid cone theory.

Average velocities can be computed from the density data, provided the static pressure and total temperature are known. For irrotational, steady, adiabatic flow of an ideal gas, the total enthalpy is constant, and at any point,

$$V = \sqrt{2c_p(T_0 - T)} \tag{9}$$

where $T_0 = T_s$.

Figure 9 shows the computed velocities compared to inviscid theory where maximum differences of 2.7% at $y = 1.17$ cm and 3% at $y = 1.87$ cm are seen. These differences amount to detecting local variations in velocity of 16 m/s relative to an average flow velocity of approximately 535 m/s.

An important consideration on the accuracy of these measurements is concern for the magnitude of the asymmetry of the

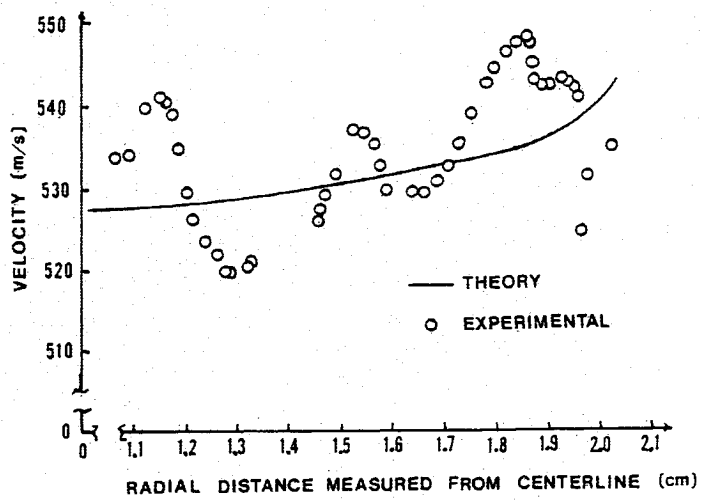

Fig. 9 Velocity distribution corresponding to data of Fig. 7.

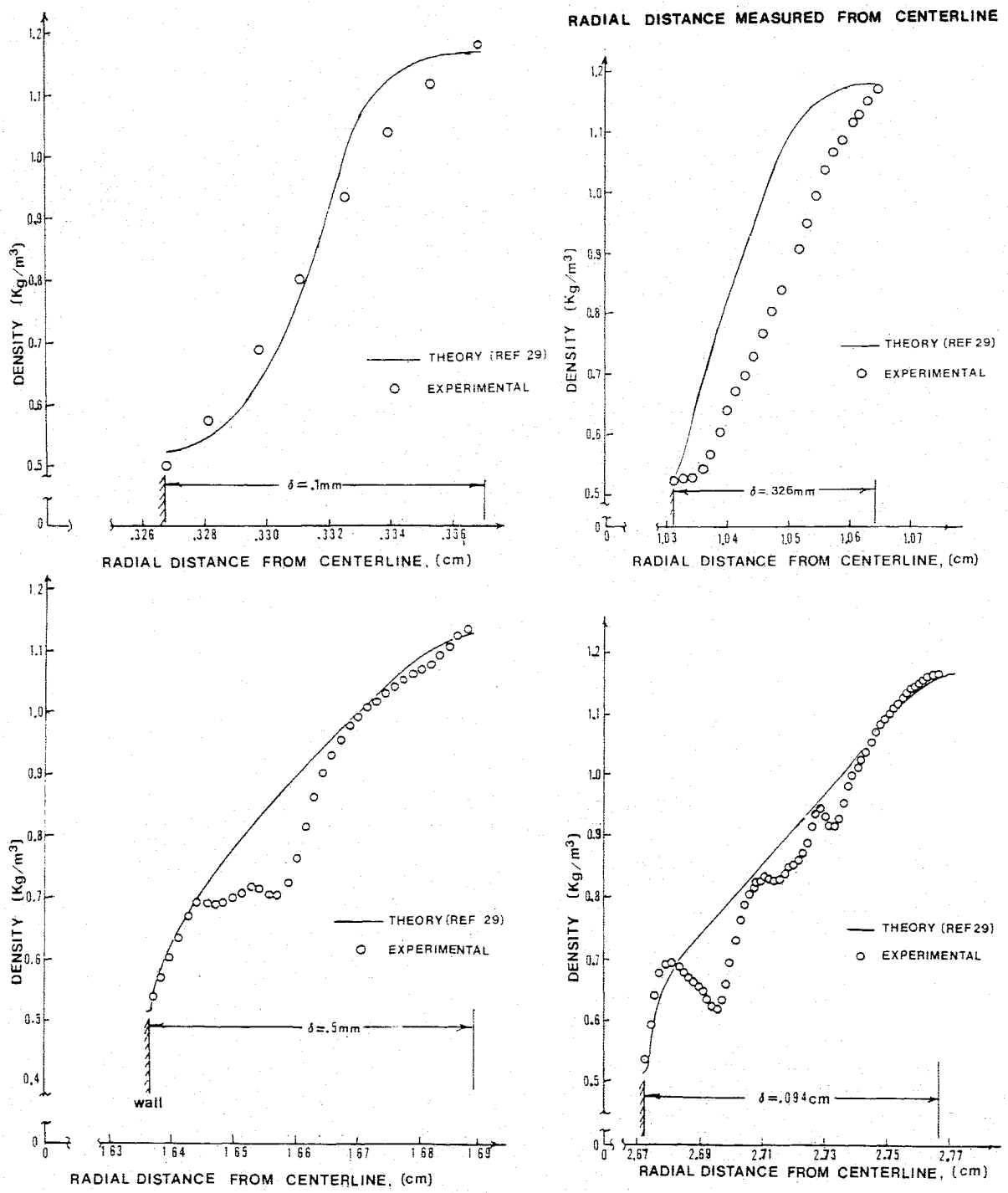

Fig. 10 Density distributions for boundary-layer segments for flowfield of Fig. 3.

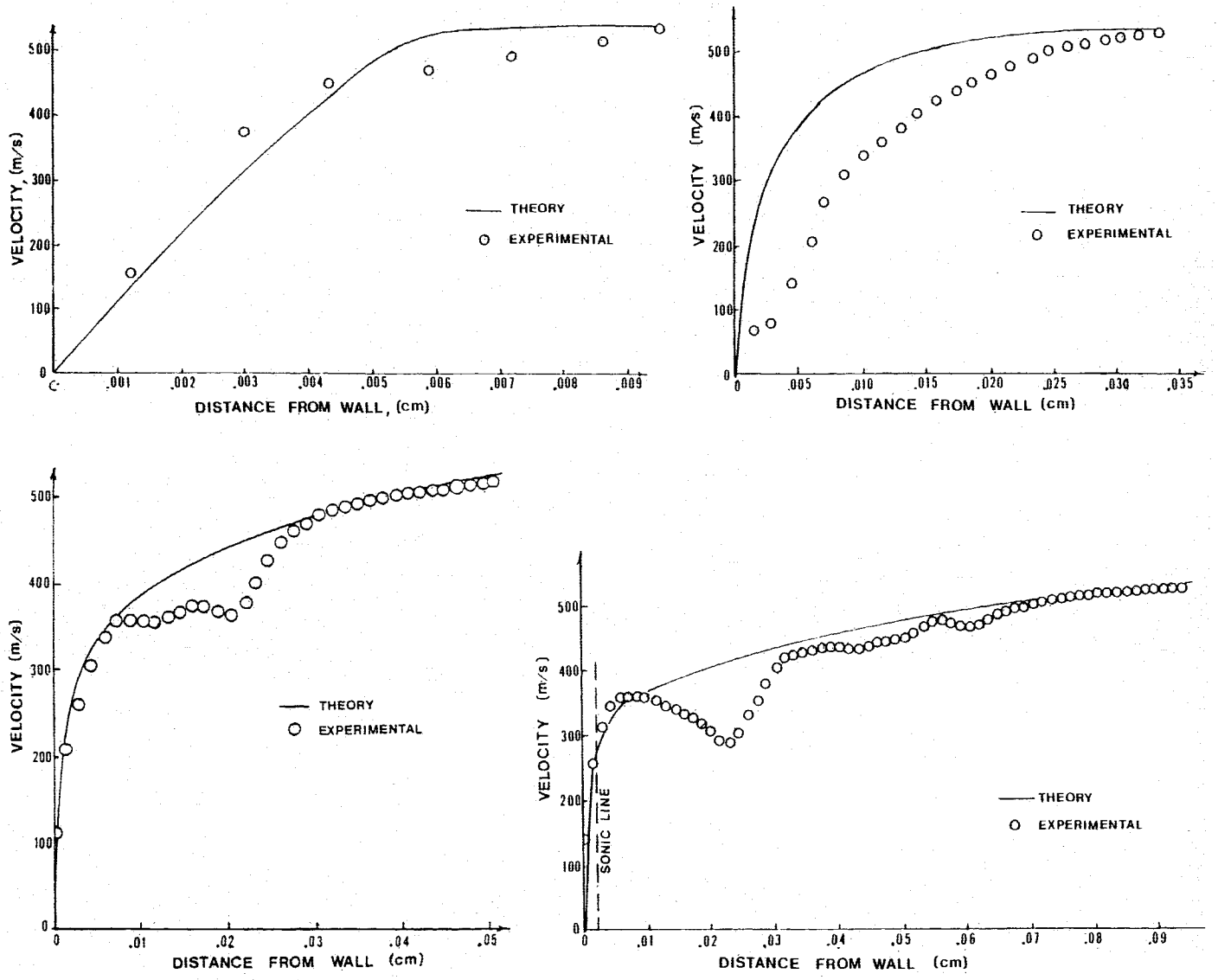

Fig. 11 Boundary-layer velocity distributions reduced from density data of Fig. 10.

unsteadiness and its affect on the S data. The flowfield is no longer axisymmetric when turbulent eddies are present, which means none of these data-reduction methods is valid. However, with only one view of the field available, data reduction can be done using only methods applicable to axisymmetric fields. Hence, the concern is: How much asymmetry is allowed before the axisymmetric assumption is invalid for data reduction? Experimentally, this question is unresolvable now, because no practical way exists to obtain instantaneous, multiple views of these flowfields. If we use a semitheoretical process called computational interferometry,[6] asymmetric disturbances are predicted to cause large errors in reduced data even for small and seemingly decaying disturbances. A precise error band depends on the size, strength, and location of the disturbances. In one example where the disturbance is centered in Region II so as to cause a local 10% deviation in the normal $S(y)$ distribution, as much as a 20% error in density is computed. However, on the basis of the small disagreement with the theory for the data of Region II, the effects of the asymmetric eddies do not appear too influential here. Finally, note that because data reduction involves curve fitting, difficulties inherently occur at the extremities of the fields where there are no points beyond the end values that can help determine the coefficients of the numerical functions. This difficulty is evident at both y_e and y_w, and for these cases, a 3 to 5% error in the computed density is anticipated using Eqs. (6) and (7); the error is normally much greater using the other data-reduction methods, because the error in $S'(y)$ is usually much larger.

Boundary-Layer Flowfield Results

The thin boundary layer, Region I, is seen in Fig. 4 by the fringes of Region II turning backward to the left. Typically, the thickness of the laminar boundary layer for these studies is 0.1 mm or less, whereas that for the turbulent boundary layer is on the order of 1.0 to 1.5 mm. As shown, the fringe configurations of each region are visibly different. For the laminar region, the fringes are nearly parallel to the surface of the cone, whereas for the turbulent flow, the fringes are steep. For the flows of this study, $T_w/T_{aw} \simeq 1$, and ρ_e and ρ_w are invariant, which means the sharp lateral bending of the fringes in the laminar region is due to the small thickness of the boundary layer. The increased thickness of the turbulent boundary layer corresponds to an increase in the optical path lengths (the secants increase), and hence the fringe shifts are much greater. Also, the fringes of the turbulent region contain irregularities that are the visible result of instantaneous recordings of turbulent eddies in the flow.

Quantitative data of the boundary layer are obtained for four X_c planes: $X_c = 1.537$ cm (laminar flow), $X_c = 4.853$ cm (transition start), $X_c = 7.701$ cm (transition end), $X_c = 12.577$ cm (turbulent flow). The amount of S data measured for each

plane varies according to the boundary-layer thickness. For $X_c = 1.537$ cm, $y_e = 0.101$ mm, $S(0.101) = 0.203$, and eight data points are measured. For $X_c = 12.577$ cm, $y_e = 0.939$ mm, $S(0.939) = 1.552$, and 66 data points are measured. For the two transition cross sections, 24 and 36 data points are obtained, respectively, for $X_c = 4.853$ cm and $X_c = 7.701$ cm. The density distributions for these planes are shown in Fig. 10. The discrepancies between the theory and the measured values are due primarily to the unsteadiness of local turbulence; the theory[15] is for steady flow. The disagreement between the optical data and theory for $X_c = 4.853$ cm is due either to a premature start for the transition model in the theory or to the fact that the optical data are instantaneous measurements of an unsteady flow.

Similar to the inviscid field, the average velocity is computed from Eq. (9), but here T_0 varies. For these flows, the Crocco equation[21,22] is used to relate the total temperature to the velocity

$$T_0 = [(T_s - T_w)/V_e]\, V + T_w$$

and hence the velocity is computed from the parabola

$$V^2 - \frac{2C_pT_w}{V_e}\left(\frac{T_s}{T_w} - 1\right) V - 2C_pT_w\left(\frac{T}{T_w} - 1\right) \qquad (10)$$

where $T = p_e/R_g\rho$.

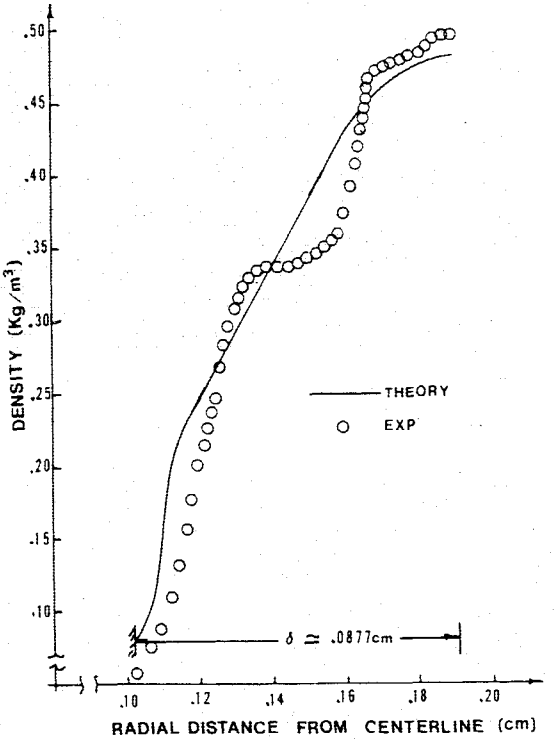

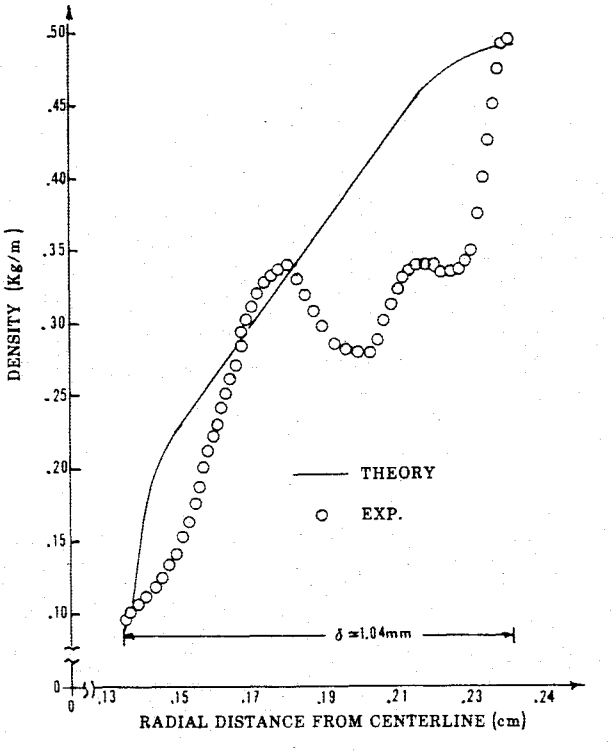

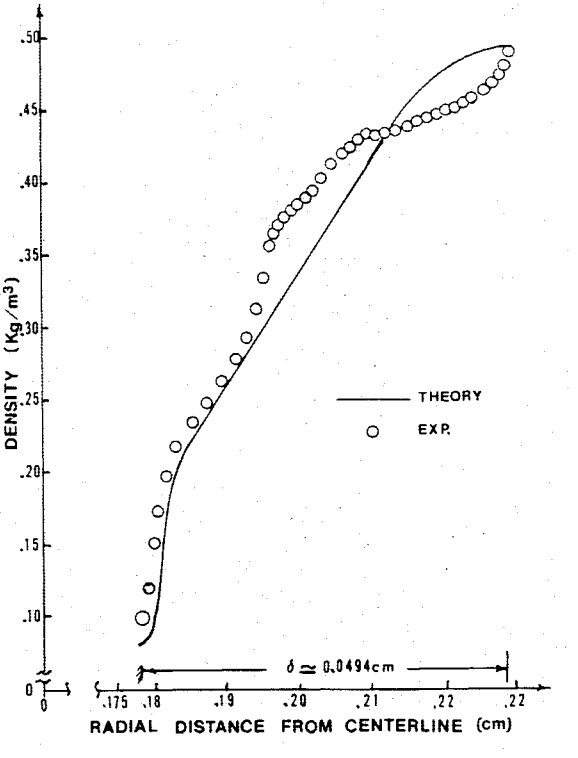

Fig. 12 Density distributions of turbulent burst of boundary layer shown in Fig. 4.

Figure 11 shows the velocity distributions for the density data of Fig. 10; V_e and p_e are obtained from inviscid cone theory, and T_w is measured with thermocouples and is nearly equal to $T_{aw} = 227.8$ K. The density computed from the optical measurements cannot be used to compute T_w because quantities at the extremities of the optical data are unreliable. Nonetheless, if we assume that only the wall value and the next point immediately away from the wall are in error, accurate flowfield densities are measurable to within 30 μm of the wall; if only the wall value is rendered erroneous, then the data are known to within 15 μm of the wall.

Application to Turbulent Bursts

Although general data of bursting are reported in the literature,[16-20] two major problems appear to exist in obtaining quantitative data of supersonic flows: 1) knowledge a priori on burst formation is unknown, which means obtaining an optical record of a burst is by chance; naturally generated bursts are transient and sporadic and are believed to travel at 40 to 70% of the freestream velocity,[17] and 2) the burst appears to be asymmetric, which makes the reduction of the interferometric measurements using methods applicable to axisymmetric flows questionable.

References 19 and 20 report on the bursting associated with boundary-layer transition along the surface of an axisymmetric ogive body placed in a subsonic flow. Motion-picture smoke visualizations distinctly show the periodic formation of axisymmetric vortex rings, as well as the formation and propagation of Tollmien–Schlichting waves. These structures appear to be axisymmetric and dependent on the local Reynolds number. The authors report that for their higher Reynolds number studies ($Re \sim 10^6$), the formation of the waves is continuous and is generally followed by a vortex-truss pattern analogous to bursting. The smoke visualizations show the vortex-trusses to be axisymmetric.

The apparent axisymmetric structure of bursting is not seen in the present supersonic airflow study. Unfortunately, similar time-dependent visualizations are not possible because adequate optical resolution using high-speed motion pictures could not be obtained. Instead, instantaneous holographic exposures of repeated tests are made in the hope that bursting will be seen in at least several of the holograms. This approach does reveal bursting, and one of the better results is presented in Ref. 11. However, none of the optical recordings here shows an axisymmetric burst. Rather, all results show the bursts to be an asymmetric instantaneous local state of the boundary layer, which is also the same result often seen in the shadowgrams of different projectiles in supersonic flight in ballistic ranges. Also unfortunate for the present study is the single line-of-sight restriction, which means the geometric shape of the bursts cannot be defined. Nonetheless, if we use only the single line-of-sight views of these structures, an effort is made to determine quantitative descriptions from the interferograms because the results are notably different from any other boundary-layer distributions seen before.

For the burst reported in Ref. 11, the boundary layer is laminar immediately in front of the burst, and y_c is 0.1 mm. Within the burst, the boundary-layer thickness increases suddenly to approximately 1.0 mm, after which it decreases to 0.6 mm. Faintly visible in the central portion of the Schlieren photograph[11] is a thin dark segment that is approximately 0.15 mm wide and 3 mm long. This darkened region shows a reversal of the density gradient, which suggests the presence of a vortex-type structure. Furthermore, the fringe structure for this boundary-layer region has never been seen before. As illustrated in the accompanying interferogram, this fringe forms a steplike shape that definitely shows the presence of a strong density gradient. Figure 12 depicts three density distributions through this burst. To the left and right of the steplike fringe ($X_c = 11.685$ cm and 20.385 cm), the distributions are similar to those of a turbulent boundary layer, whereas the results for the steplike fringe at $X_c = 15.550$ cm show a sudden decrease in the density, followed immediately by a rapid increase.

An important concern for the validity of these density data is reiterated. The optical data are valid interferometric measurements of the flow for the specific line of sight used to see the burst. With only one view of the flow available, exact reduction of the optical data to density is not possible. Since the burst is an asymmetric field and the degree of the asymmetry is unknown, the results presented in Fig. 12 are questionable. If the asymmetric structure of the burst is not too dissimilar from an overall axisymmetric configuration, then these density data are reasonable.

Conclusions

Three contributions are made by this study. First, new and unique optical measurements of supersonic boundary-layer flows are presented. Second, a data-reduction method that minimizes amplification of scatter in interferometric measurements of axisymmetric flowfields is presented. Third, a special application of discrete phase-shift interferometry using the dual hologram technique is combined with a direct viewing, fringe-reading process to obtain nearly continuous measurements of the fringe shifts. Application of this technique is demonstrated by measuring fringe shifts in a thin laminar boundary layer, where the total fringe shift is much less than one, and again by obtaining more than 20 times the data normally available from the interferogram of a turbulent boundary layer. The credibility of the reduction of these measurements lies in the accuracy of the axisymmetric flowfield assumption. For truly axisymmetric flows, the reduction leads to results that are within 3% of theory. Elsewhere, the error found in using axisymmetric techniques to reduce measurements of asymmetric fields can be more than 20%, depending on the magnitude of the asymmetry. The findings on the application to turbulent burst are new and unique and definitely indicate that more research and improved optical surveying are required to understand these flowfield structures.

Acknowledgments

The author acknowledges the generous support provided throughout this study by the Computational Fluid Dynamics Group, the High Speed Aerodynamics Branch, the Instrumentation Branch, all of the Air Force Flight Dynamics Laboratory, Air Force Wright Aeronautical Laboratories, Wright-Patterson Air Force Base, Dayton, Ohio.

References

[1]Bennett, F. D., Carter, W. C., and Bergolt, V. E., "Interferometric Analysis of Airflow About Projectiles in Free Flight," *Journal of Applied Physics,* Vol. 23, April 1952, pp. 453-469.

[2]Vest, C. M., *Holographic Interferometry,* Wiley, New York, 1979.

[3]Barr, W. L., "Method for Computing the Radial Distribution of Emitters in a Cylindrical Source," *Journal of the Optical Society of America,* Vol. 52, Aug. 1962, pp. 885-887.

[4]Bradley, J. W., "Density Determination from Axisymmetric Interferograms," *AIAA Journal,* Vol. 6, June 1968, pp. 1190-1192.

[5]Hildebrand, B. B., *Methods of Applied Mathematics,* 2nd ed., Prentice-Hall, Englewood Cliffs, NJ, 1965, p. 276.

[6]Havener, A. G. and Obergefell, L. A., "Computational Interferometric Description of Nested Flow Fields," *Optical Engineering,* Vol. 24, No. 3, May-June 1985, pp. 441-445.

[7]Trolinger, J. D., "Laser Instrumentation for Flow Field Diagnostics," *AGARDograph,* Vol. 186, March 1974.

[8]Havener, A. G. and Radley, R. J., Jr., "Turbulent Boundary Layer Flow Separation Measurements Using Holographic Interferometry," *AIAA Journal,* Vol. 12, Aug. 1974, pp. 1071-1075.

[9]Havener, A. G., "Users Guide on Pulse Laser Holography for Wind Tunnel Testing," Aerospace Research Lab., Wright-Patterson AFB, Dayton, OH, ARL TR75-0123, AD/A 017710, June 1975.

[10]Hannah, B. W. and King, W. L., Jr., "Extensions of Dual Plate Holographic Interferometry," *AIAA Journal,* Vol. 15, May 1977, pp. 725-727.

[11]Havener, A. G., "Detection of Boundary Layer Transition Using Holography," *AIAA Journal,* Vol. 15, April 1977, pp. 592-593.

[12]Vest, C. M., "Information Retrieval from Holographic Interferograms—Fundamentals and Problems," *Automated Reduction of Data from Images and Holograms,* NASA Ames Research Ctr., Moffett Field, CA, NASA Conference Publication 2477, Jan. 1985, pp. 5-6.

[13]Trolinger, J. D., "The Holography of Phase Objects," *Proceedings of the 31st SPIE Annual Technical Symposium,* SPIE, The International Society for Optical Engineers, Bellingham, WA, Aug. 1987.

[14]Modarrass, D. and Azzazy, M., "Modern Experimental Techniques for High Speed Flow Measurements," AIAA Paper 88-0420, Jan. 1988.

[15]Shang, J. S., Hankey, W. L., Jr., and Dwoyer, D. L., "Numerical Analysis of Eddy Viscosity Models in Supersonic Turbulent Boundary Layer," *AIAA Journal,* Vol. II, Dec. 1973, pp. 1677-1683.

[16]Emmons, H. W., "The Laminar-Turbulent Transition in a Boundary Layer—Part 1," *Journal of the Aeronautical Sciences,* Vol. 18, July 1951, pp. 490-498.

[17]James, C. S., "Observations of Turbulent-Burst Geometry and Growth in Supersonic Flow," NACA TN 4235, April 1958.

[18]Wygnanski, I., Sokolow, M., and Friedman, D., "On the Spot in a Boundary Layer Undergoing Transition," Air Force Office of Scientific Research, Bolling AFB, Washington, DC, AFOSR TR 75-1385, ADA 015389, 1975.

[19]Mueller, T. J., Nelson, R. C., Kegelman, J. T., and Morkovin, M. V., "Smoke Visualization of Boundary-Layer Transition on a Spinning Axisymmetric Body," *AIAA Journal,* Vol. 19, Dec. 1981, pp. 1607-1608.

[20]Kegelman, R. C., Nelson, R. C., and Mueller, T. J., "The Boundary Layer on an Axisymmetric Body With and Without Spin," *AIAA Journal,* Vol. 21, Nov. 1983, pp. 1485-1491.

[21]Schetz, J. A., *Foundations of Boundary Layer Theory for Momentum Heat and Mass Transfer,* Prentice-Hall, Englewood Cliffs, NJ, 1984, pp. 96-99.

[22]White, F. M., *Viscous Flow,* McGraw-Hill, New York, 1974, pp. 627-629.